Effect of d electrons on defect properties in equiatomic NiCoCr and NiCoFeCr concentrated solid solution alloys

Shijun Zhao, Takeshi Egami, G. Malcolm Stocks, and Yanwen Zhang

Effect of *d* electrons on defect properties in equiatomic NiCoCr and NiCoFeCr concentrated solid solution alloys

Shijun Zhao[1], Takeshi Egami[1,2,3], G. Malcolm Stocks[1], Yanwen Zhang[1,2]

[1] *Materials Science and Technology Division, Oak Ridge National Laboratory, Oak Ridge, TN 37831, USA*

[2] *Department of Materials Science and Engineering, University of Tennessee, Knoxville, TN 37996, USA*

[3] *Shull Wollan Center – Joint Institute for Neutron Sciences and Department of Physics and Astronomy, University of Tennessee, Knoxville, TN 37996, USA*

Abstract

The role of d electrons in determining distributions of formation and migration energies for point defects in equiatomic NiCoCr and NiCoFeCr concentrated solid solution alloys (CSAs) are studied regarding electron density deformation flexibility based on first-principles calculations. The disordered state is taken into account by constructing special quasirandom structures. The migration barriers are determined by directly optimizing the saddle point. It is found that the formation energies of interstitials in CSAs are lower than those in pure Ni, whereas the formation energies of vacancies are higher. In both NiCoCr and NiCoFeCr, Co-related dumbbell interstitials exhibit lower formation energies. Notably, the distributions of migration energies for Cr interstitials and vacancies exhibit exponential decay. A detailed analysis of the electronic properties reveals that the electronic charge deformation flexibility regarding e_g to t_{2g} transition has a dominant effect on defect energetics of different elements in CSAs. Thus the electron deformation ability is suggested as a key factor in understanding the peculiar defect behavior in CSAs.

1. Introduction

Because of their exceptional mechanical properties and irradiation resistance, concentrated solid solution alloys (CSAs) with multiple principal elements situated in a simple face-centered cubic (*fcc*) or body-centered cubic (*bcc*) lattice have received extensive attention [1–3]. It has been experimentally demonstrated that the irradiation resistance of CSAs is strongly correlated with the number of elements in the alloys and the corresponding elemental compositions [2,4,5]. In other words, the underlying disordered state that is inherent to CSAs plays an essential role in determining their irradiation performance. The disorder in CSAs is a consequence of random arrangement of different elements and the resulting random distributions of induced local magnetic moments and associated small site-to-site displacement fluctuations. Previous studies have shown that disorder in CSAs helps to reduce electron mean free path and further decrease electrical and thermal conductivity, which leads to slow energy dissipation and enhanced radiation resistance [2,5]. It has also been proposed that lattice strains at the atomic level produced by different species occupying the same lattice modify defect formation and migration energies, leading to easier melting and possibly enhancing healing of defects under ion irradiation [6]. Nevertheless, how the underlying disordered state contributes to the enhanced irradiation resistance is still not clear [4,5,7].

Under ion irradiation, large number of interstitials and vacancies are created. Our previous studies have demonstrated that the disorder in CSAs has a significant influence on defect energetics [8]. Specifically, formation and migration energies of defects in CSAs exhibit distributions since they are strongly dependent on local environment. The characterization of defect energies is fundamental to the understanding of elemental-specific defect properties. In addition, defect diffusion, the main mechanism responsible for the microstructure evolution, is intimately related to defect energetics [9,10]. Therefore, studying defect energetics in CSAs is a prerequisite to developing theoretical models for predicting the elemental segregation and precipitation behavior in CSAs [11].

For the most studied *fcc* CSAs comprised of 3*d* transition metals, their lattice symmetries are well preserved, despite the underlying chemical disorder [12]. The introduction of defects into CSAs breaks the lattice symmetry. Therefore, the flexibility of electrons to accommodate additional defects is important to understanding defect behavior. The electron deformation ability of specific elemental component is related to their electronic structures. For example, Ni has a nearly full *d*-shell, indicating that electron density around Ni atoms is rigid and hence, difficult to be deformed even under strikingly different environments. On the other hand, the partially filled *d*-shells of Cr and Fe may provide additional deformation flexibility of electrons and make the migration of corresponding defects easier.

In this work, defect energetics in two equiatomic multi-component CSAs, NiCoCr and NiCoFeCr, are studied using *ab initio* calculations. The formation and migration energies of interstitials and vacancies are calculated. The chemical disorder is taken into account by constructing special quasirandom structures (SQS) [13]. The saddle configurations are directly optimized in order to calculate migration barriers. The determined defect energy distributions are presented and discussed with respect to *d* electron properties. It is found that defect migration can be understood in terms of inhomogeneous electronic charge distribution through electron transfer between e_g and t_{2g} states.

2. Method

First-principles calculations were based on the density-functional theory as implemented in the Vienna *ab initio* simulation package (VASP) [14]. A gradient corrected functional in the Perdew-Burke-Ernzerhof (PBE) form was used to describe the exchange and correlation interactions [15]. Electron-ion interactions were treated within the projector-augmented-wave (PAW) method [16]. The energy cutoff (E_{cut}) for the plane-wave basis set was set to be 270 eV and the energy convergence criterion was set to be 10^{-4} eV. The

4

convergence of energy cutoff used in this work was tested by calculating interstitial formation energies in Ni using different E_{cut} values. The calculated formation energy of an interstitial in pure Ni was 3.96 eV at E_{cut}=270 eV. Further increase of E_{cut} to 400 eV gave rise to 4.02 eV, which suggests that the uncertainty of our results is less than 0.1 eV. These results are in line with previous studies which indicate that the uncertainty of formation energies in Ni-Fe-Cr alloys is around 0.1 eV [17]. Nevertheless, the formation energy differences converge much faster (0.05 eV). Therefore, our results are reliable when comparing formation energies of different defect types. Most importantly, migration barriers, which are calculated as energy differences, are barely affected by this uncertainty. Note that similar energy cutoff was also used in previous works to study defect properties in Fe-Ni-Cr alloys [18]. All calculations were performed with spin-polarization to allow full relaxation of magnetic moments. The initial magnetic moments for each element were initialized according to their average moments obtained from coherent potential approximation calculations [19]. After optimization, it turns out that Ni, Co and Fe sites are coupled ferromagnetically (FM) with themselves and each other, whereas Cr sites prefer to couple antiferromagnetically (AFM) with other Cr sites as well as Ni, Co and Fe sites. Defect calculations were performed within a 256-atoms supercell, using a Gamma-point-based 2×2×2 mesh to sample the Brillouin zone. The chemical disorder was modelled using SQS structures that were constructed by optimization of the Warren-Cowley short range order (SRO) parameters [20,21] using a Monte-Carlo simulated annealing algorithm [22]. The calculation of electronic properties was performed with a fine K-points mesh of 4×4×4. This computational setting corresponds to 16384 kpoints·atom, which has been proved to yield converged electronic DOS [23].

The defect formation energy is calculated from:

$$E_f = E_d - E_0 \pm \mu_d \,, \tag{1}$$

where μ_d is the chemical potential of the defect species d, E_d and E_0 are the energies of defective and defect-free supercells respectively. The chemical potential is a measure of the energy variation when a

specific atom is added to or removed from the host material. In pure metals or dilute alloys, the chemical

potential is usually taken as the energy per atom of the corresponding elemental solid. In concentrated

disordered alloys, it is expected that the elemental chemical potential is different from those in pure metal.

Following our previous method [8], the elemental chemical potentials were estimated by calculating the

energy difference when substituting an A atom with B atom. Then the energy differences were averaged

by taking into account elemental composition of the first nearest neighbor shell around the A atom. The

averaged energy difference was taken as the chemical potential difference $\mu_A - \mu_B = E^{A->B} - E_0$. In this way,

the chemical potential for each element can be determined.

Migration barriers of defects were calculated by directly optimizing saddle point configurations. For

interstitials and vacancies in a perfect *fcc* lattice, their saddle structures are located at the mid-point of

their diffusion paths, as identified from nudged elastic band (NEB) calculations in pure Ni [8]. In CSAs,

the disorder will lead to a small deviation from the ideal mid-point position. By optimizing this saddle

structure using the quasi-Newton method with direct inversion in the iterative subspace (DIIS) algorithm

[24], its local minimum can be located. The migration barrier can then be obtained from the energy

difference between the saddle structure and defective structure:

$$E_m = E_s - E_d , \qquad (2)$$

where E_s and E_d are the energy of the saddle structure and the stable defect structure, respectively.

3. Result

It has been shown that the most stable interstitial defects in pure Ni are [100] dumbbells [25]. Therefore,

we concentrate on this type of interstitials. The migration of a [100] interstitial dumbbell in pure Ni is via

conversion to a [010] dumbbell involving a rotation mechanism [8,25]. In this diffusion path, the saddle

structure contains the interstitial located at the mid-point of the path. In this work, this structure is used as the starting configuration to calculate the saddle point energy in pure Ni and the considered CSAs. To illustrate the calculation process, the optimized initial, saddle and final states for a Ni interstitial in NiCoCr are provided in Figure 1. In the initial state, the Ni interstitial shares the lattice position with a Ni atom, creating a [100] Ni-Ni dumbbell. The final state contains a [010] Ni-Cr dumbbell formed by the Ni interstitial with a Cr atom located at a first-nearest-neighbor site from the initial dumbbell's center. For this transition, the saddle state occurs when the Ni interstitial occupies approximately the mid-point of the path, while the Ni atom in the original dumbbell undergoes small displacement toward its original lattice site and the Cr atom in the nearest site is displaced from its ideal lattice position. The energy difference between the saddle and initial state (E_s–E_i) as well as the energy difference between the saddle and final state (E_s–E_f) are determined as the migration barrier of the Ni interstitial. The migration of vacancies is through hopping between nearest-neighbor-sites. This process is equivalent to the hopping of a lattice atom. Therefore, the saddle structure of this transition is when the lattice atom occupies the mid-point between the two nearest-neighbor lattice sites.
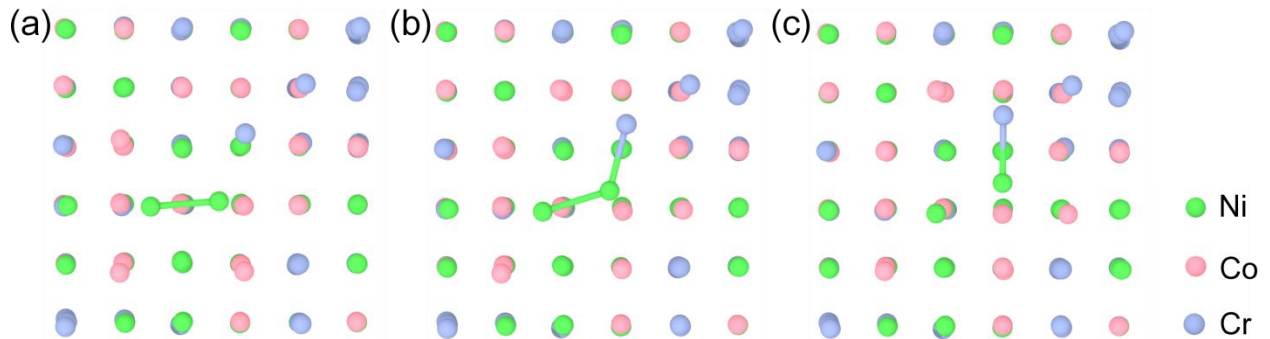
Figure 1 Illustration of the transition process of a Ni interstitial in NiCoCr from a [100] Ni-Ni dumbbell to a [010] Ni-Cr dumbbell viewed from {100} plane: (a) Initial state, (b) transition state, (c) final state.

To verify the calculation details, defect properties in pure Ni are studied first and compared to previous results. The calculated defect formation energies are 3.96 and 1.45 eV for interstitials and vacancies, respectively. These results are in good agreement with the previous results of 4.07 and 1.43 eV [8,25].

The determined migration barriers by directly optimizing saddle structures are 0.15 and 1.04 eV for interstitials and vacancies, respectively. These values are also in excellent agreement with previous NEB calculations, which yield 0.14 eV for interstitials and 1.08 eV for vacancies [8,25]. The agreement suggests that direct optimization of saddle structures is a reliable approach to calculate migration barriers.

While migration barrier calculations are independent of chemical potentials, the formation energy of defects should be calculated using elemental specific chemical potentials. The determined chemical potentials for each element are provided in Table I, together with the values calculated using their corresponding pure metals as references. For ease of comparison, the calculated cohesive energies for each metal are also provided. Standard errors of the calculated chemical potentials in alloys are also shown, which are estimated from the average of substitutional energy differences. The largest standstard error is only 0.06 eV for Fe and Cr, which may be arised from their complex magnetisms (AFM) compared to Ni and Co (FM). It is shown that chemical potentials of Ni in these two CSAs are lower than those in pure *fcc* FM Ni. However, chemical potentials of other elements are a little higher than those in their corresponding pure metal phases. This conclusion is not affected even after taking into account of the standard error associated with elemental chemical potentials in alloys. The calculated mixing energies are 0.25 and 0.30 eV per formula unit for NiCoCr and NiCoFeCr, respectively. The positive mixing energies suggest that these two *fcc* CSAs are enthalpically metastable at 0 K based on *ab initio* calculations. Indeed, previous results show that for disordered NiCoCr and NiCoFeCr CSAs, their *hcp* phases are more enthalpically favorable than *fcc* phases [22]. Nevertheless, the energy difference is very small. Since the relevant structures for both alloys at finite temperature are *fcc* phases, we choose their *fcc* structures to calculate defect energetics. Although temperature may induce variation to defect energetics, the general trend as discussed in this study is not likely to be influenced. On the other hand, the positive mixing energies also indicate possible short range order in these alloys.

Table I Calculated elemental chemical potentials in alloys and pure metals. For comparison, cohesive energies (E_{coh}) for corresponding pure metals are also given. All energies are in eV/atom.

	NiCoCr	NiCoFeCr	Pure metal	E_{coh}
μ_{Ni}	-5.50±0.02	-5.53±0.02	-5.46[a]	4.78
μ_{Co}	-6.97±0.03	-6.99±0.02	-7.03[b]	5.14
μ_{Cr}	-9.27±0.06	-9.22±0.03	-9.50[c]	4.06
μ_{Fe}		-8.18±0.06	-8.24[d]	4.85

[a] *fcc* FM Ni.
[b] *hcp* FM Co.
[c] *bcc* AFM Cr.
[d] *bcc* FM Fe.

The calculated formation energies of [100] interstitial dumbbells and vacancies in NiCoCr and NiCoFeCr are shown in Figure 2. For both systems, it is found that the formation energies of interstitials are all lower than those in pure Ni (3.96 eV). In NiCoCr, consideration of various possible dumbbell pairs reveals that Co-Co and Co-Cr dumbbells have, generally, lower formation energies than Ni-Ni dumbbells. These results suggest preferable binding of interstitials in NiCoCr. As a result, the diffusion of interstitials will rely on these preferable diffusion channels, leading to higher diffusion coefficients of Co and Cr interstitials, as shown by *ab initio* molecular dynamics simulations [10]. In NiCoFeCr, Co-Co, Co-Fe and Co-Cr dumbbells exhibit lower formation energies among all the dumbbells studied, indicating preferable binding of Co interstitials.
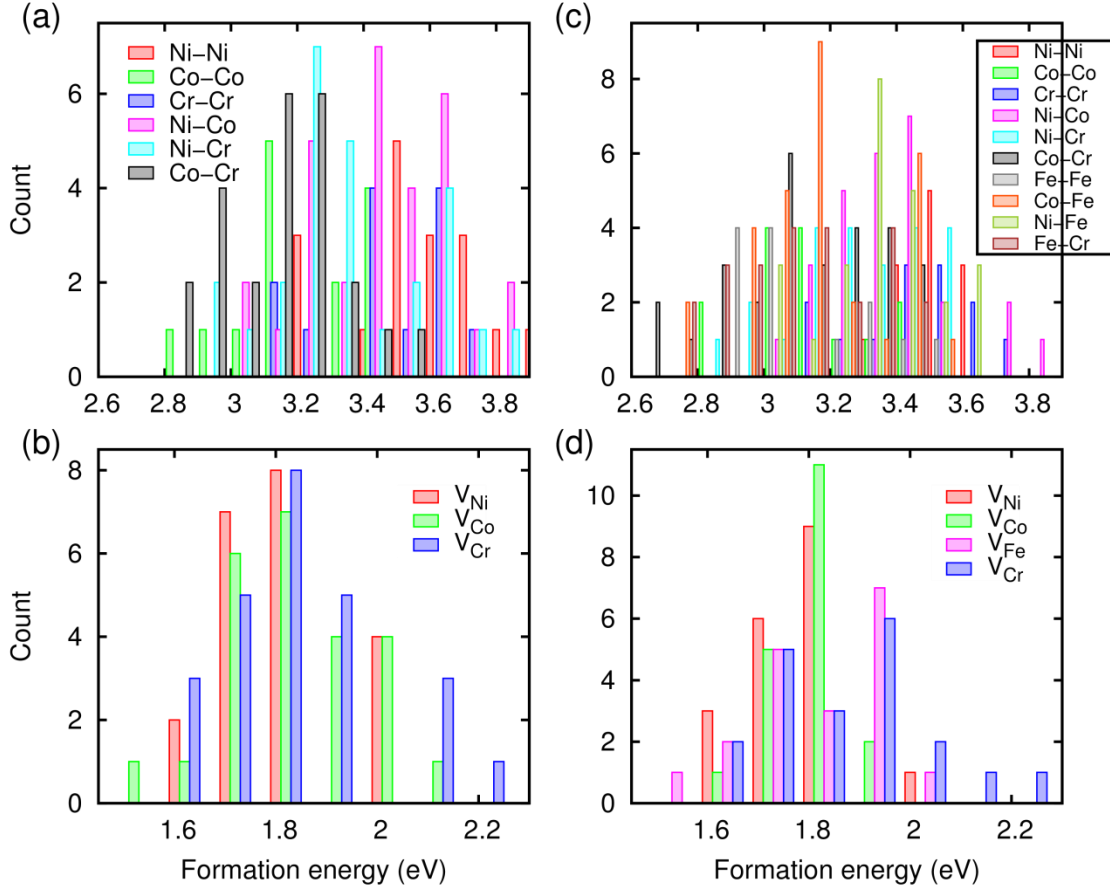
Figure 2 Calculated formation energies of interstitials and vacancies in NiCoCr and NiCoFeCr: (a) formation energies of interstitials in NiCoCr, (b) formation energies of vacancies in NiCoCr, (c) formation energies of interstitials in NiCoFeCr and (d) formation energies of vacancies in NiCoFeCr.

For vacancies, Figure 2 shows that their formation energies in both NiCoCr and NiCoFeCr are all higher than those in pure Ni (1.45 eV). In NiCoCr, Cr vacancies have higher formation energies among the three vacancy types. An inspection of the first-nearest neighbor (1nn) shell surrounding the vacancies, as provided in Figure 3, reveals that the more Ni atoms in the 1nn shell, the lower formation energy of vacancies, similar to the observation in NiCo and NiFe [8]. Another observation is that the formation energy of vacancies increases with increasing Co and Cr atoms in the 1nn shell. These results suggest that vacancies prefer Ni-rich as well as Co-poor and Cr-poor environments. Similar conclusion is also found

10

in Ni-Fe-Cr alloys, which can be attributed to strong binding interactions between Ni and vacancies [26]. In NiCoFeCr, Figure 2 shows that the formation energies of Cr vacancies are higher than other vacancies. An analysis of the atomic compositions around the vacancies reveals the same trend as observed in NiCoCr: vacancies favor Ni-rich and Co and Cr-poor environments, as shown in Figure 3.
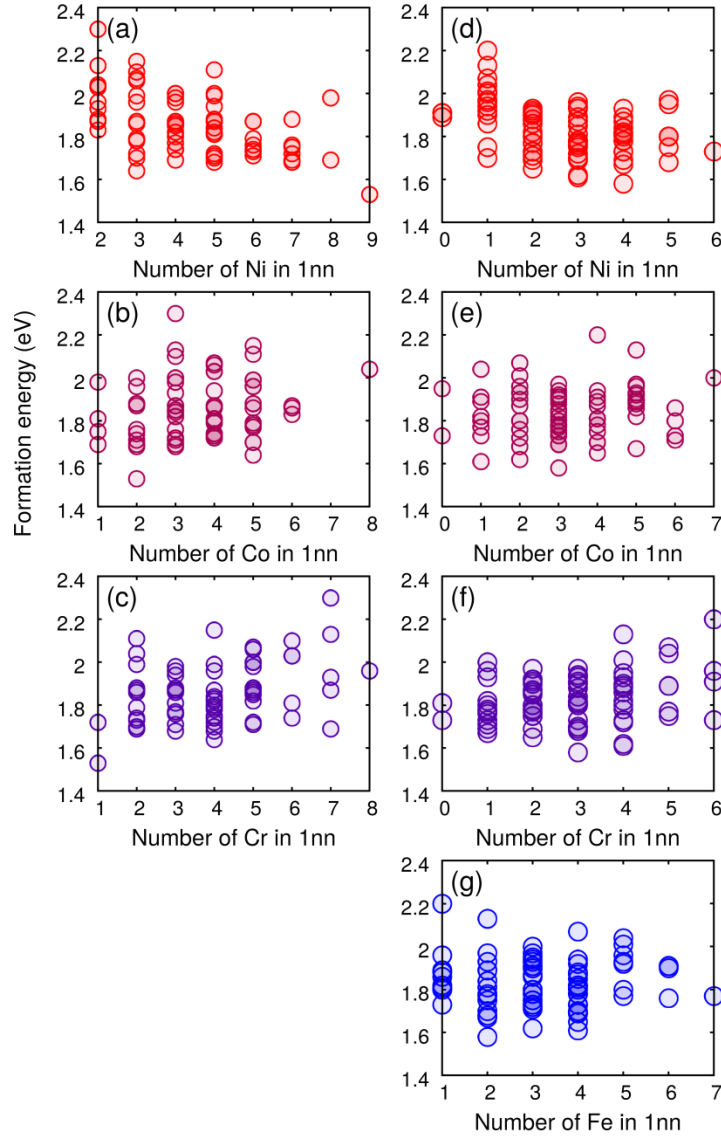
Figure 3 Dependence of vacancy formation energies on their atomic environments in the first nearest neighbor shell for NiCoCr (left column) and NiCoFeCr (right column).

Migration barriers in NiCoCr and NiCoFeCr are presented in Figure 4. The results indicate that migration barriers of interstitials in CSAs are mostly larger than those in pure Ni (0.15 eV), indicating slower diffusion process for interstitials. For vacancies, a large fraction of the barriers in NiCoCr and NiCoFeCr are lower than those in pure Ni (1.04 eV). Notably, the distributions of migration barriers for different interstitial dumbbells are mixed in both alloys. As a result, preferable binding of interstitial dumbbells is the main mechanism in determining preferable diffusion of interstitials. On the other hand, migration barriers for vacancies are separated for different species. In particular, Cr vacancies exhibit lower migration barriers in both NiCoCr and NiCoFeCr, which suggests preferable diffusion of Cr vacancies.
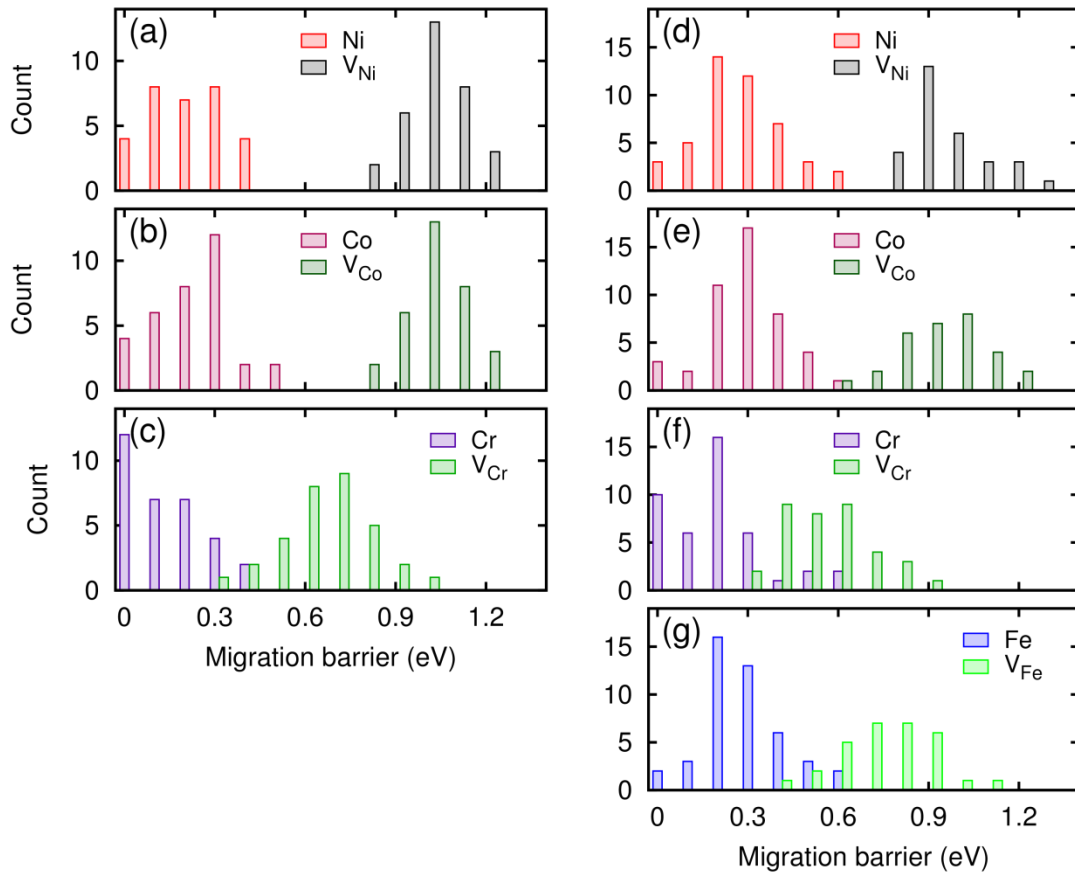
Figure 4 Migration barriers of interstitials and vacancies in NiCoCr (left column) and NiCoFeCr (right column).

Figure 4 shows that there is a large overlap region between migration energies for interstitials and vacancies, especially for Cr interstitials and vacancies. The overlap in migration energies may lead to enhanced defect recombination and annihilation because of strong interactions between interstitials and vacancies. To study the distinct behavior of Cr defects, the underlying electronic structures are analyzed in terms of their electronic density of states (DOS) and electron density distributions. For the alloys studied here, their DOS are dominated by d electrons. In addition, distributions of s-p electrons are little influenced by alloy structure. For the present purpose, it is therefore sufficient to focus on the atomic species projected DOS (PDOS) from d electrons, which can be further decomposed into t_{2g} and e_g symmetries (components). In order to show evolution of DOS after introduction of defects, we provide in Figure 5 the PDOS change for different elements in NiCoCr after a Cr interstitial is added. The evolution of decomposed PDOS averaged at three randomly chosen Cr (the first row), Ni (the second row) and Co (the third row) atomic sites are given. The three columns in Figure 5 represent PDOS of the original atom in the perfect cell, PDOS of the original atom in the dumbbell and PDOS of the introduced Cr interstitial in the dumbbell, respectively. Figure 5 indicates that in the perfect structure, more electrons occupy t_{2g} states than e_g states because of local lattice symmetry of the fcc structure. After the introduction of a Cr interstitial creating a Cr-Cr dumbbell that breaks the fcc symmetry, the occupation of e_g states is increased whereas that of t_{2g} states is decreased, so that the occupations of t_{2g} states and e_g states are almost equal for all Cr atoms in the dumbbell structures, as indicated by Figure 5(c), (f) and (i). On the other hand, the occupation number of Ni and Co contributed from t_{2g} and e_g states changes little upon the formation of dumbbell defects, as seen in Figure 5(e) and (h) from the small changes in the encompassed area by t_{2g} and e_g PDOS below the Fermi energy.
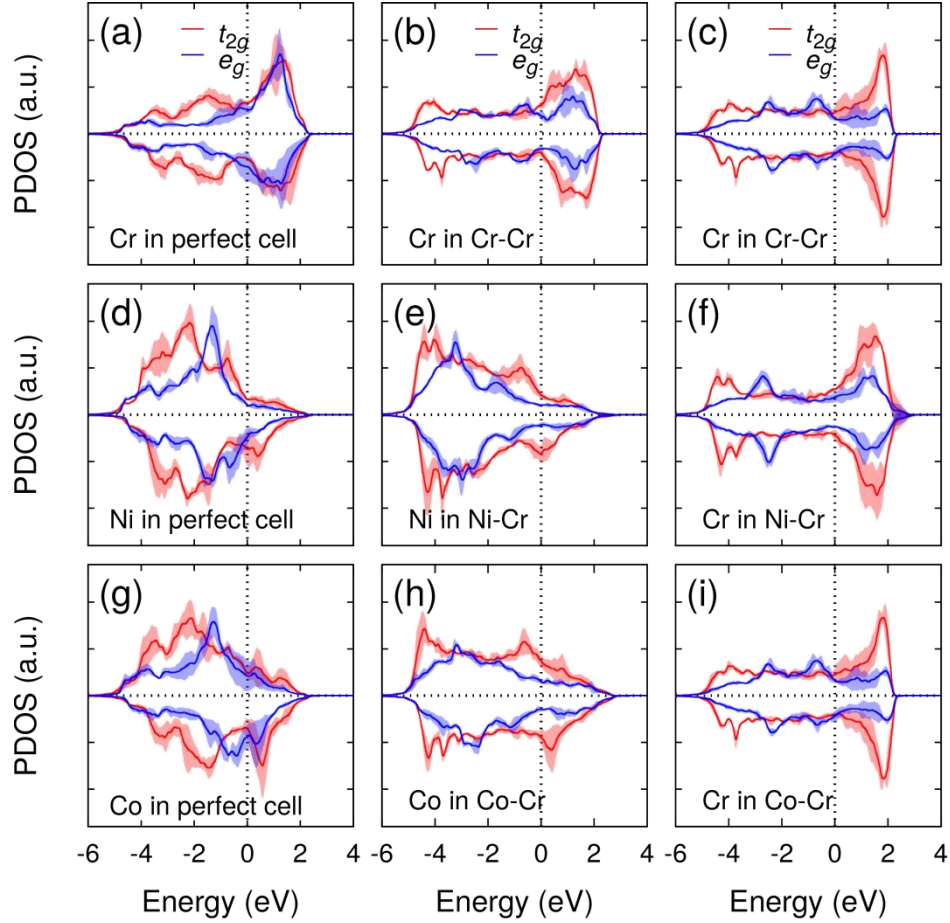
Figure 5 Projected density of states (PDOS) of a Cr interstitial in NiCoCr introduced at a randomly chosen Cr (the first row), Ni (the second row) and Co (the third row) atomic site. The three columns represent PDOS of the original atom in the perfect cell, PDOS of the original atom in the dumbbell and PDOS of the introduced Cr interstitial in the dumbbell, respectively. Fermi level is located at 0 eV. In each case, PDOS from three randomly chosen defect sites are averaged and the standard deviation is represented by shaded area.

More information on the d electron properties can be gained from electron density distributions. The charge density arising from the occupied electronic states in perfect NiCoCr as well as a Cr dumbbell are

shown in Figure 6 in the {100} plane. In the perfect structure, Figure 6(b) shows that the electron density of Cr atoms exhibits a quadrilateral shape, instead of spherical distribution found in Ni and Co atoms. The density of Cr extends along the diagonal direction with respect to the orthogonal simulation box, which suggests typical t_{2g}-like orbitals, whereas the spherical distribution around Ni and Co atoms suggests $(t_{2g}+e_g)$-like orbitals. When a [100] Cr-Cr dumbbell is formed, Figure 6(d) shows that the charge density on the Cr atoms around the defects changes to e_g-like features (along axial direction), whereas the densities of Ni and Co atoms are not much influenced as indicated in Figure 6(d). When the Cr interstitial migrates to the nearest Ni atom, the saddle structure is created (Figure 6(e)). On this occasion, the orbitals of Cr atoms change directions whereas those of Ni and Co remain almost the same. Finally, a [010] Cr-Ni dumbbell is produced, with e_g-like orbitals in Cr atoms and almost unaltered orbitals in Ni and Co atoms (Figure 6(h)). The flexibility of Cr orbitals originates from its partially-filled nature, as demonstrated in the PDOS. The transition from t_{2g} to e_g symmetry in Cr atoms is a result of the lowered symmetry due to the introduction of defects.
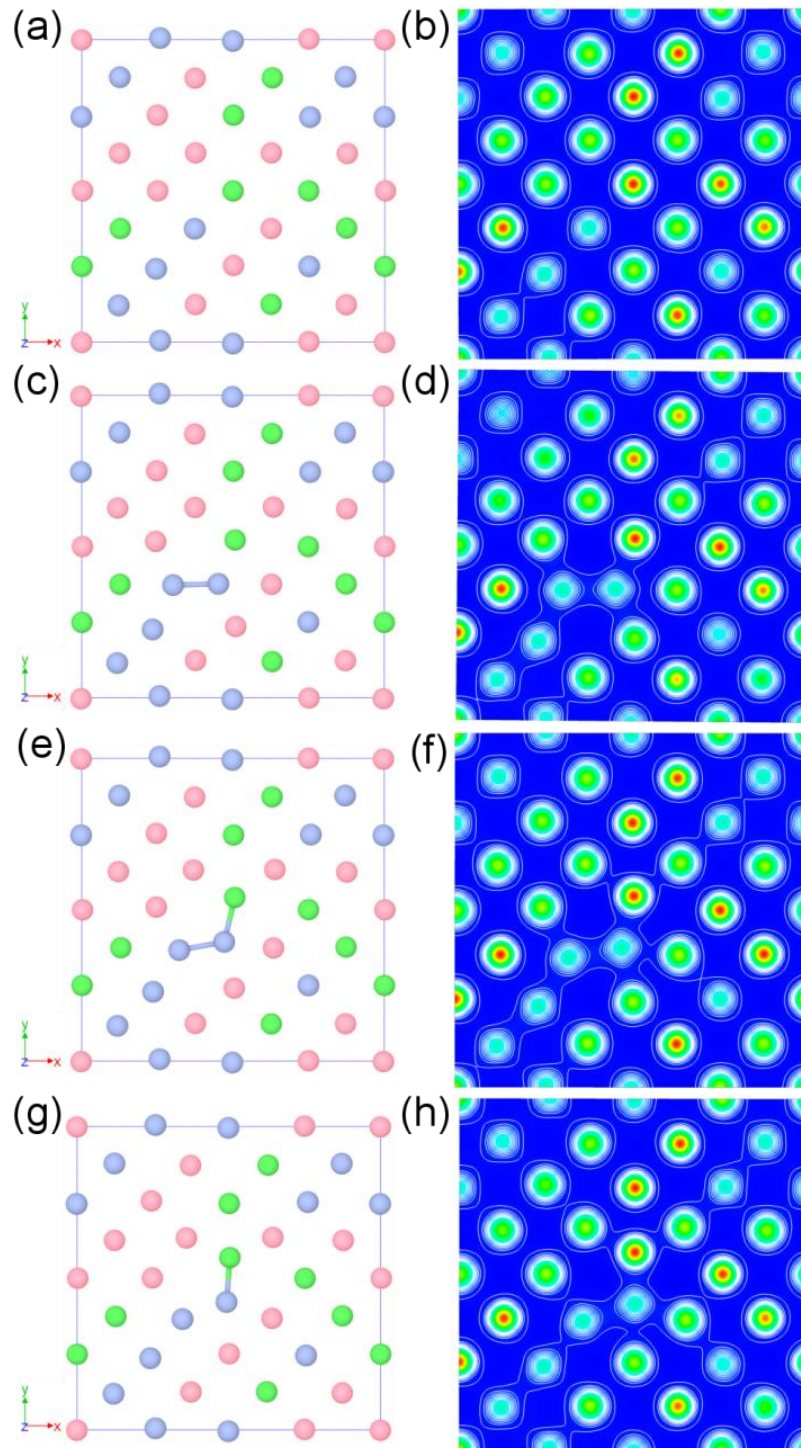
Figure 6 The atomic configuration in a {100} plane and the corresponding electron density for occupied states. (a–b) perfect structure, (c–d) Cr-Cr dumbbell, (e–f) saddle structure and (g–h) Cr-Ni dumbbell.

Similar results are also observed in NiCoFeCr, in which Cr is dominated by e_g orbitals after the introduction of defects. The d-electron numbers in the t_{2g} and e_g decomposed states are tabulated in Table II for defect-free cell and the defective structure after introduction of a Cr interstitial. These data are calculated by integration of PDOS as shown in Figure 5. Here only one randomly chosen defect site is considered. It shows that the electron number of the t_{2g} character in Ni is slightly enhanced. For Fe and Co, the e_g character is enhanced instead, resulting in a net electron from t_{2g} orbitals to e_g orbitals. On the other hand, Ni strongly resists charge deformation to accommodate the defect. It is worth pointing out that these values are calculated by integrating PDOS within an atomic sphere. We have tested the influence of used spherical radius on the calculated PDOS and only minor effects are found even after taking into account of the reduction of Wigner-Seitz radius for the interstitial dumbbell atoms (see Appendix for details).

Table II Typical values of t_{2g} and e_g decomposed d-electron numbers for each element in defect-free and defective supercells after introduction of a Cr interstitial.

		Defect-free		Defective		Difference	
		t_{2g}	e_g	t_{2g}	e_g	$\Delta(t_{2g})$	$\Delta(e_g)$
NiCoCr	Ni	4.80	3.41	5.00	3.35	0.20	-0.06
	Co	4.25	2.91	4.30	3.07	0.05	0.16
	Cr	2.55	1.45	2.27	2.07	-0.28	0.62
NiCoFeCr	Ni	4.89	3.42	5.05	3.37	0.16	-0.05
	Co	4.36	2.96	4.35	3.11	-0.01	0.15
	Fe	3.88	2.38	3.71	2.82	-0.17	0.44
	Cr	2.66	1.49	2.38	2.06	-0.28	0.57

Table II shows d-electron occupation in t_{2g} and e_g orbitals for each element in defect-free and defective structures, which provides information on electronic structure evolution after defect formation. For defect migration, the migration barriers are determined by the energy difference between the saddle and final states. Therefore, it is important to identify the change in the electronic structure when the defect moves from a stable site to a saddle point. To this end, the changes in the electron occupation are calculated and

presented in Figure 7, together with the associated energy barriers. The changes in the electron occupation from the t_{2g} to e_g states can be expressed by:

$$\Delta\rho = [\Delta\rho(e_g) - \Delta\rho(t_{2g})]/2, \tag{3}$$

where $\Delta\rho(t_{2g})$ and $\Delta\rho(e_g)$ are the changes in the total occupation of the t_{2g} and e_g states between the saddle and final states, respectively. Figure 7 shows that Cr exhibit the largest $\Delta\rho$, along with a wide distribution of migration barriers. Variations in $\Delta\rho$ are smaller for Ni because the d-band of Ni is nearly full, and the variation is also small for Co, for which d-band is more than 80% full. The relation between the changes in electron orbital occupation and the barrier heights demonstrates that large variation of $\Delta\rho$ in Cr makes it very flexible so that its migration barriers exhibit wide distributions. This effect may be characterized as electronic flexibility.
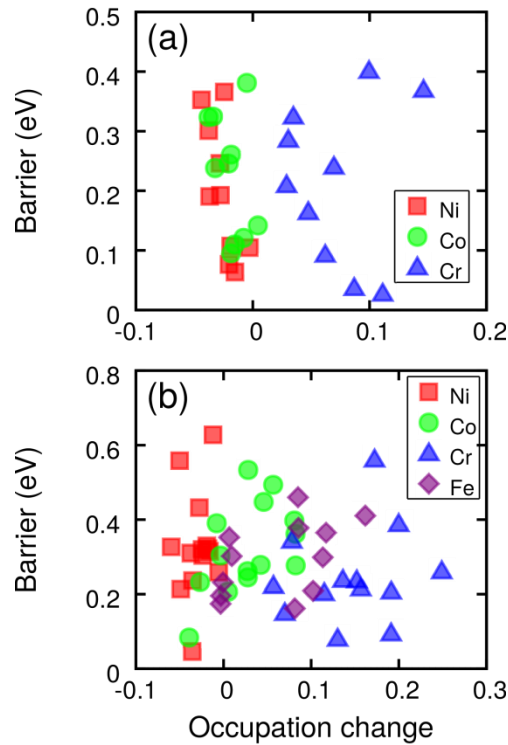
Figure 7 Migration energy barriers as a function of changes in electron occupation from the t_{2g} to the e_g state: (a) interstitials in NiCoCr; (b) interstitials in NiCoFeCr.

Based on the electronic structure analysis, it is suggested that the difference in charge deformation flexibilities of various elements is responsible for their different migration barriers presented in Figure 4. Because Cr shows the largest flexibility, the migration energies of Cr interstitials and vacancies are widely distributed compared to other defect types. Note that Cr tends to be AFM ordering [17,27,28], which is also a manifest of its flexible electronic occupation. This factor also contributes to its wide distribution of migration energies. For Ni, the charge re-distribution is insignificant due to its nearly full shell d electrons. The wide distribution of migration barriers found in Cr and Fe induces significant overlap between migration barriers for vacancies and interstitials, which may play key roles in enhancing defect recombination. Therefore, our conclusions help to reveal different roles of alloying element in concentrated alloys (high entropy alloys) in governing defect evolution.

4. Conclusions

First-principles calculations have been performed to investigate the formation and migration energies of point defects in NiCoCr and NiCoFeCr equiatomic CSAs. It is found that elemental-specific deformation flexibility of d electrons has significant impact on the defect energetics. The formation energies of interstitials in CSAs are lower than those in pure Ni, whereas the formation energies of vacancies are higher. In addition, a large overlap region between the migration barrier of interstitials and vacancies is observed in CSAs. These results suggest possible enhanced interactions between interstitials and vacancies in CSAs, which may facilitate the defect recombination and annihilation. The migration energies of different elements are analyzed regarding the flexibility of the electronic charge deformation and it is demonstrated that the ability to transfer electrons from the e_g to t_{2g} states is a key in governing the defect migration energy in NiCoCr and NiCoFeCr CSAs.

Acknowledgment

Appendix

In our calculations, the default atomic radii as provided in PAW pseudopotential files were used to calculate PDOS and occupation number of electrons. The possible errors induced by different sphere radii used for projection are analyzed in this section. To this end, the Voronoi tessellation method [29] was used to calculate the Wigner-Sitz radius of each species based on the optimized supercells. The obtained radii in perfect and defective NiCoCr supercells containing a Cr-Cr dumbbell are given below:

Table III Atomic radii of each species in NiCoCr as found in PAW pseudopotential and calculated using the Voronoi tessellation method.

		Perfect		Defective	
	Default (Å^3)	Volume (Å^3)	Radius (Å)	Volume (Å^3)	Radius (Å)
Ni	1.286	11.07	1.383	11.06	1.382
Co	1.302	10.94	1.377	10.90	1.376
Cr	1.323	11.04	1.381	11.00	1.380
Cr dumbbell				9.70	1.323

As shown in Table III, the volume surrounding the Cr atoms inside the dumbbell is smaller than that of other Cr atoms. By manually setting the RWIGS-tag in VASP calculations, we have compared the influence of modified radius on the calculated PDOS. The results are shown in Figure 8, which suggests

minor differences induced by different atomic sphere radii. Hence, the main conclusion in this study is not affected. However, the atomic sphere approximation used here may lead to some uncertainties. Since there is no easy method to calculated PDOS in a non-spherical region, we adopt sphere approximation to analyze electronic properties. Taking into account the big changes in PDOS of Cr atoms and the small influence of different projected radii, our conclusions are not likely to be affected by this approximation, though the quantities presented in Table II may be slightly affected.
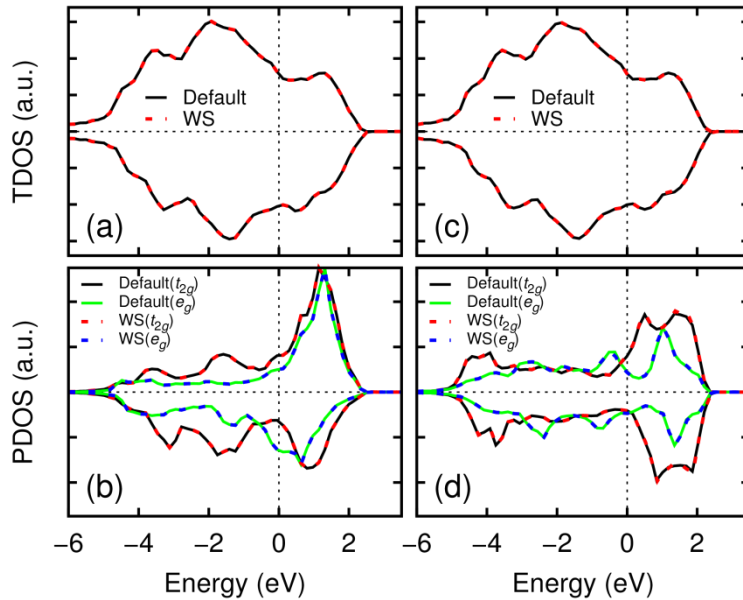
Figure 8 Dependence of calculated total DOS (TDOS) and PDOS on the used Wigner Seitz radius for perfect (left column) and defective (right column) NiCoCr supercells. The PDOS are calculated in a randomly chosen Cr atom before (b) and after (d) introduction of a Cr-Cr interstitial dumbbell.

Reference

[1]   B. Gludovatz, A. Hohenwarter, D. Catoor, E.H. Chang, E.P. George, R.O. Ritchie, A fracture-resistant high-entropy alloy for cryogenic applications, Science (80-.). 345 (2014) 1153–1158.

[2]   Y. Zhang, G.M. Stocks, K. Jin, C. Lu, H. Bei, B.C. Sales, L. Wang, L.K. Béland, R.E. Stoller, G.D.

Samolyuk, M. Caro, A. Caro, W. J. Weber, Influence of chemical disorder on energy dissipation and defect evolution in concentrated solid solution alloys, Nat. Comm. 6 (2015) 8736.

[3]   T. Egami, M. Ojha, O. Khorgolkhuu, D.M. Nicholson, G.M. Stocks, Local Electronic Effects and Irradiation Resistance in High-Entropy Alloys, JOM. 67 (2015) 2345–2349.

[4]   Y. Zhang, K. Jin, H. Xue, C. Lu, R.J. Olsen, L.K. Beland, M.W. Ullah, S. Zhao, H. Bei, D.S. Aidhy, G.D. Samolyuk, L. Wang, M. Caro, A. Caro, G.M. Stocks, B.C. Larson, I.M. Robertson, A.A. Correa, W.J. Weber, Influence of chemical disorder on energy dissipation and defect evolution in advanced alloys, J. Mater. Res. 31 (2016) 2363–2375.

[5]   Y. Zhang, S. Zhao, W.J. Weber, K. Nordlund, F. Granberg, F. Djurabekova, F. Granbergc, F. Djurabekova, Atomic-level Heterogeneity and Defect Dynamics in Concentrated Solid-Solution Alloys, Curr. Opin. Solid State Mater. Sci. (2017) https://doi.org/10.1016/j.cossms.2017.02.002.

[6]   T. Egami, W. Guo, P.D. Rack, T. Nagase, Irradiation Resistance of Multicomponent Alloys, Metall. Mater. Trans. A. 45 (2014) 180–183.

[7]   S. Zhao, W.J. Weber, Y. Zhang, Unique Challenges for Modeling Defect Dynamics in Concentrated Solid-Solution Alloys, JOM. 69 (2017) 2084–2091.

[8]   S. Zhao, G.M. Stocks, Y. Zhang, Defect energetics of concentrated solid-solution alloys from ab initio calculations: $Ni_{0.5}Co_{0.5}$, $Ni_{0.5}Fe_{0.5}$, $Ni_{0.5}Fe_{0.5}$ and $Ni_{0.5}Cr_{0.5}$, Phys. Chem. Chem. Phys. 18 (2016) 24043–24056.

[9]   Y.N. Osetsky, L.K. Béland, R.E. Stoller, Specific features of defect and mass transport in concentrated fcc alloys, Acta Mater. 115 (2016) 364–371.

[10]   S. Zhao, Y. Osetsky, Y. Zhang, Preferential diffusion in concentrated solid solution alloys: NiFe, NiCo and NiCoCr, Acta Mater. 128 (2017) 391–399.

[11]   M.-R. He, S. Wang, S. Shi, K. Jin, H. Bei, K. Yasuda, S. Matsumura, K. Higashida, I.M. Robertson, Mechanisms of radiation-induced segregation in CrFeCoNi-based single-phase concentrated solid solution alloys, Acta Mater. 126 (2017) 182–193.

[12]   D.B. Miracle, O.N. Senkov, A critical review of high entropy alloys and related concepts, Acta

Mater. 122 (2017) 448–511.

[13]   A. Zunger, S.-H. Wei, L.G. Ferreira, J.E. Bernard, Special quasirandom structures, Phys. Rev. Lett. 65 (1990) 353.

[14]   G. Kresse, J. Furthmüller, Efficiency of ab-initio total energy calculations for metals and semiconductors using a plane-wave basis set, Comput. Mater. Sci. 6 (1996) 15–50.

[15]   J.P. Perdew, K. Burke, M. Ernzerhof, Generalized gradient approximation made simple, Phys. Rev. Lett. 77 (1996) 3865.

[16]   P.E. Blöchl, Projector augmented-wave method, Phys. Rev. B. 50 (1994) 17953.

[17]   T.P.C. Klaver, D.J. Hepburn, G.J. Ackland, Defect and solute properties in dilute Fe-Cr-Ni austenitic alloys from first principles, Phys. Rev. B. 85 (2012) 174111.

[18]   J.D. Tucker, R. Najafabadi, T.R. Allen, D. Morgan, Ab initio-based diffusion theory and tracer diffusion in Ni–Cr and Ni–Fe alloys, J. Nucl. Mater. 405 (2010) 216–234.

[19]   Z. Wu, M.C. Troparevsky, Y.F. Gao, J.R. Morris, G.M. Stocks, H. Bei, Phase stability, physical properties and strengthening mechanisms of concentrated solid solution alloys, Curr. Opin. Solid State Mater. Sci. 21 (2017) 267–284.

[20]   J.M. Cowley, Short-range order and long-range order parameters, Phys. Rev. 138 (1965) A1384.

[21]   J.M. Cowley, An approximate theory of order in alloys, Phys. Rev. 77 (1950) 669.

[22]   S. Zhao, G.M. Stocks, Y. Zhang, Stacking fault energies of face-centered cubic concentrated solid solution alloys, Acta Mater. 134 (2017) 334–345.

[23]   X. Zhang, B. Grabowski, F. Körmann, C. Freysoldt, J. Neugebauer, Accurate electronic free energies of the 3d, 4d, and 5d transition metals at high temperatures, Phys. Rev. B. 95 (2017) 165126.

[24]   P. Pulay, Convergence acceleration of iterative sequences. the case of scf iteration, Chem. Phys. Lett. 73 (1980) 393–398.

[25]   J.D. Tucker, T.R. Allen, D. Morgan, Ab Initio Defect Properties for Modeling Radiation-Induced Segregation in Fe-Ni-Cr Alloys, 13th Environ. Degrad. Mater. Nucl. Power Syst. (2007).

[26] J.B. Piochaud, T.P.C. Klaver, G. Adjanor, P. Olsson, C. Domain, C.S. Becquart, First-principles study of point defects in an fcc Fe-10Ni-20Cr model alloy, Phys. Rev. B. 89 (2014) 24101.

[27] R. Hafner, D. Spišák, R. Lorenz, J. Hafner, Magnetic ground state of Cr in density-functional theory, Phys. Rev. B. 65 (2002) 184432.

[28] T.P.C. Klaver, R. Drautz, M.W. Finnis, Magnetism and thermodynamics of defect-free Fe-Cr alloys, Phys. Rev. B. 74 (2006) 94435.

[29] C.H. Rycroft, VORO++ : A three-dimensional Voronoi cell library in C++, Chaos An Interdiscip. J. Nonlinear Sci. 19 (2009) 41111.